electricity

MDPI

Article

Preselective Ground Fault Detection Using Vector Reactive Asymmetry in Hierarchical Relay Protection Automation Environments

Zhanat Issabekov [1], Vladyslav Romashchenko [2], Dmitry Kachan [2], Batyrbek Ordabayev [1,*], Bibigul Issabekova [1], Olzhas Talipov [1] and Didar Bayev [1]

[1] Faculty of Energy, Department of Electrical Engineering and Automation, Toraighyrov University, Lomov Street 64, Pavlodar 140008, Kazakhstan; isabekov.g@teachers.tou.edu.kz (Z.I.); issabekova.b@teachers.tou.edu.kz (B.I.)

[2] Department of Electrical, Mechanical and Industrial Engineering, Hochschule Anhalt, Anhalt University of Applied Sciences, 06366 Kothen, Germany; vladyslav.romashchenko@hs-anhalt.de (V.R.); dmitry.kachan@hs-anhalt.de (D.K.)

* Correspondence: ordabaev.bat@students.tou.edu.kz; Tel.: +7-707-9437400

Abstract

While multi-phase short circuits are reliably cleared by conventional overcurrent relays, single-phase-to-ground faults (SPGFs) in isolated, compensated, or resistance-grounded 6–10 kV distribution networks produce extremely low, highly distorted currents that frequently cause traditional zero-sequence protections to misoperate. Because SPGFs constitute the vast majority of network disturbances, resolving this specific low-current detection challenge remains a critical priority for grid resilience. This paper presents a preselective protection approach based on Vector Analysis of Reactive Asymmetry Current (VARAC), designed for implementation in digital relay protection and automation terminals. Instead of relying primarily on vulnerable zero-sequence quantities, the method derives diagnostic features from the reactive asymmetry structure of three-phase current phasors. A reactive asymmetry matrix is formed from pairwise imaginary cross-products, symmetrized to preserve real eigenvalues and stable modal interpretation. The dominant eigenvalue and eigenvector are then used to quantify fault intensity and directional skew through two decision features: a magnitude-based index and a normalized asymmetry ratio. This enables robust discrimination between normal and faulted operation, including low-current and compensated-fault conditions where conventional criteria lose sensitivity. Simulation and oscillographic evaluations show a clear separation between pre-fault and SPGF regimes, fast onset detection, and improved structural selectivity versus traditional zero-sequence indicators. The proposed algorithm is computationally lightweight and compatible with hierarchical distributed SCADA architectures, supporting coordinated monitoring, diagnostics, and adaptive protection functions in modern medium-voltage networks.

Keywords: single-phase-to-ground fault (SPGF); reactive asymmetry; VARAC index; fault direction detection; medium-voltage distribution networks; relay protection and automation (RPA); eigenvalue-based fault analysis; digital protective relaying; arc-suppression reactor (ASR) networks; hierarchical distributed SCADA

Check for updates

Academic Editors: Bo Yang and Lin Jiang

Received: 28 May 2026
Revised: 15 July 2026
Accepted: 22 July 2026
Published: 24 July 2026

Copyright: © 2026 by the authors. Licensee MDPI, Basel, Switzerland. This article is an open access article distributed under the terms and conditions of the Creative Commons Attribution (CC BY) license.

1. Introduction

Modern power systems require highly resilient and reliable electricity supplies to consistently meet strict power quality standards [1,2]. The increasing performance require-

ments imposed on modern protection and control systems are driven by the zero-tolerance continuity needs of automated industrial processes, a growing proliferation of sensitive loads, and the rapid integration of Distributed Energy Resources (DERs) [3]. These operational challenges are particularly acute in medium-voltage (1–35 kV) distribution networks, where accurate fault detection and localisation remain technically challenging in various grid configurations (see Figure 1).

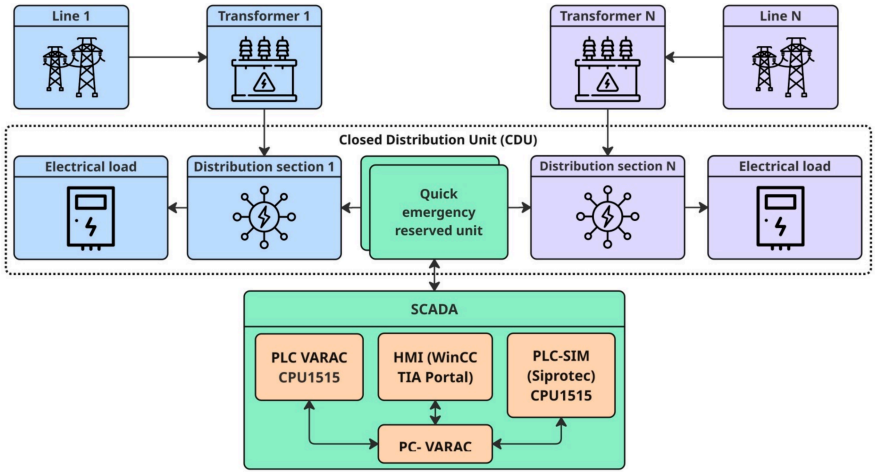


Figure 1. A Distribution Network Unit (DNU) within a Hierarchical SCADA Architecture.

Within these 1–35 kV distribution networks, network disturbances are broadly categorised by their physical behaviour. Multi-phase faults—including phase-to-phase, double-phase-to-ground, and three-phase short circuits—are characterised by low-impedance pathways and high short circuit currents. Consequently, these severe events are reliably and instantaneously cleared by conventional phase overcurrent protection (OCP) or distance relays. In contrast, single-phase-to-ground faults (SPGFs) constitute approximately 70 to 80% of all network anomalies [4–6]. Unlike multi-phase short circuits, SPGFs produce extremely low fault currents, especially in resonant-grounded systems utilising Arc-Suppression Reactors (ASRs) or in isolated neutral networks. Because the resulting ground-fault current is frequently lower than the nominal load current, standard phase OCP elements are entirely blind to these disturbances, which justifies why this study focuses exclusively on SPGF detection.

The inherently variable nature, low magnitude, and unstable behaviour of ground-fault currents under high-resistance or compensated neutral regimes make their accurate detection highly problematic, particularly in networks where capacitive grounding currents dominate [7–9]. Conventional SPGF protection schemes typically rely on fundamental-frequency zero-sequence overcurrent or directional ground-fault elements that evaluate absolute amplitude thresholds or the phase relationship between residual current and voltage ($3U_0$ and $3I_0$) [10–14]. Although widely applied, these methods exhibit poor sensitivity and selectivity in isolated or compensated neutral grids because the zero-sequence quantities are severely weakened, neutralised by Petersen coils, or distorted by line capacitive imbalances and load variability [15].

To address these limitations, contemporary microprocessor-based Relay Protection and Automation (RPA) terminals are increasingly being deployed, which are capable of integrating highly sophisticated mathematical algorithms and various protective functions into a single physical device [16]. While this multi-functionality enhances local grid flexibility, optimising the overall protection system requires extensive coordinated monitoring, data sharing, and system-wide diagnostics. Consequently, there is a compelling need to

embed these advanced RPA terminals within distributed hierarchical SCADA frameworks to facilitate localised, highly sensitive, and selective fault analysis.

According to recent findings, reactive and vector-based indicators remain diagnostically effective under low fault currents and are less prone to load-induced distortions than active or zero-sequence quantities. Özveren et al. report that reactive power and phase energy-flow asymmetry remain informative in active grids, even at low short-circuit currents [17]. Arango et al. offer a straightforward fault-direction approach using active power in unbalanced three-phase systems—positive changes signify direct faults, while negative changes indicate reverse faults, so only the sign of the power change is required post-detection [18]. Zhu et al. find that the reactive current component is less affected by power-load distortions than the active component, thus serving as a stable protective feature [19].

Unlike previous studies, the present work takes into account the following:

- a preselective SPGF detection algorithm based on reactive-asymmetry vector analysis, operating without zero-sequence quantities;
- a defined KVARAC index and associated decision rule, demonstrating that the dominant eigenvector yields a stable fault-direction indicator;
- a proposed integration scheme for embedding the algorithm into microprocessor-based RPA terminals within a hierarchical distributed SCADA architecture.

The paper is organised as follows. Section 2 describes the hardware components and measurement parameters relevant to the preselective method. Section 2.2 presents the design flow and mathematical foundation. The simulation and experimental results are reported in Section 3. Finally, Section 5 provides the conclusions of the proposed approach.

2. Methodology

In 6–10 kV distribution networks, the primary goal during power outages—especially those caused by SPGF—is to maintain reliability and ensure continuity of the production process by stabilizing and restoring power supply under emergency conditions. To achieve this, it is possible to propose implementing the preselective VARAC method within an Automated Process Control System (APCS). In an industrial facility, power transmission should be regarded as a subprocess of the APCS, alongside the facility's core operations, and therefore treated as a control object. The fundamental principle of the method consists of the following steps:

- Measuring phase currents via the SIPROTEC terminal
- Transmitting the measured data to the PLC
- Performing calculations according to the VARAC algorithm
- Generating a control signal
- Activating the fast emergency reserve entry system while monitoring the current status of the protection terminals

2.1. General Representation of RPA Terminals and Measurement Equipment

To perform phase-current analysis using the preselective vector method, empirical measurements are required. These are sourced from line-entry current transformers in substations and integrated into multifunctional protection and automation platforms (e.g., Siemens SIPROTEC). Figure 2a,b shows the typical SIPROTEC hardware configuration used in these RPA applications.



(**a**) (**b**)

Figure 2. General representation of SIPROTEC hardware at industrial RPA Terminals: (**a**) view near one of the cabinets; (**b**) general view of the RPA terminal.

Modern microprocessor-based RPA terminals feature integrated fault-recording capabilities and non-volatile memory, enabling the high-resolution capture of current and voltage oscillograms [20]. The systems record instantaneous phase currents (i_A(t), i_B(t), i_C(t)), zero-sequence currents (i_N/i_{NS}), and phase voltages (v_A, v_B, v_C, $v_N/3v_0$, v_{SYN}). By employing a sliding one-cycle window with a 10–20 ms update interval, the device achieves minimal latency, albeit with increased susceptibility to signal noise. At a nominal system frequency of 50 Hz, this processing logic results in a resolution of 16 samples per cycle.

Figure 3 depicts the processing stages of Sampled Values (SAV) within the measurement acquisition chain. To satisfy the Nyquist–Shannon sampling theorem and mitigate aliasing effects, an analog low-pass (anti-aliasing) filter is integrated into the input stage.

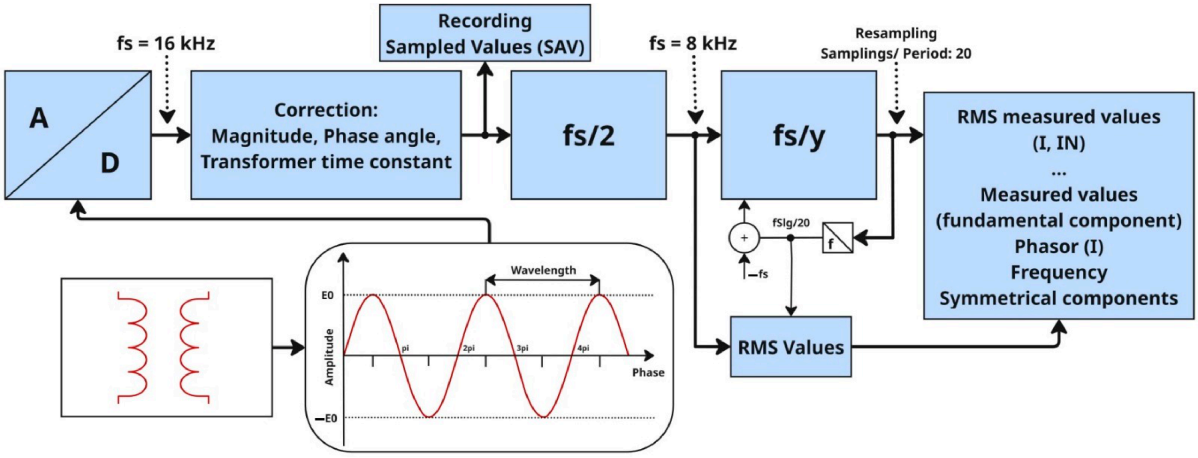


Figure 3. SIPROTEC. Measured Value Acquisition Chain. This figure is adapted from [21].

Following the sampling process, the current channels are digitally adjusted to compensate for magnitude, phase, and the transformer time constant [22]. This calibration ensures comprehensive hardware interchangeability, permitting the replacement or swapping of current transformer terminal blocks between devices without compromising measurement accuracy.

2.2. Mathematical Representation of Phasor Extraction

The projection of the tip of the rotating vector onto the coordinate axes generates sinusoidal oscillations, corresponding to the relationship $i = I_m \cdot \sin(\omega t)$. In this model, every instantaneous current value i is uniquely defined by the temporal correlation between time t and the phase angle ωt. To empirically validate this conceptual framework, independent

measurements were performed across multiple RPA terminals. The geometric basis of the signal is shown in Figure 4.

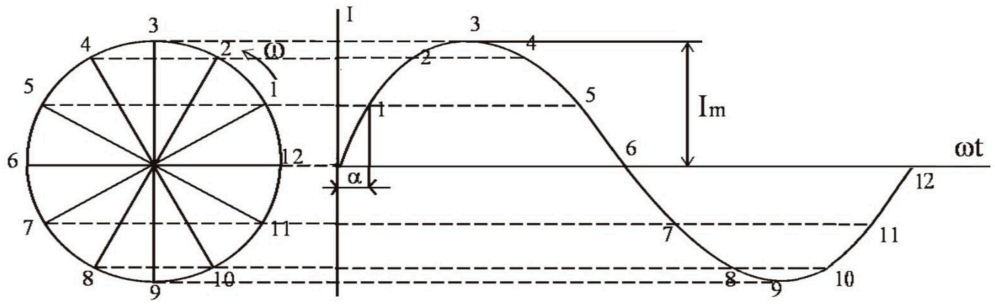


Figure 4. Rotating vector representation of sinusoidal wave [23].

As described in the hardware section, the system operates on the assumption of a quasi-steady signal within the analysis window, centered at a nominal frequency of 50 Hz. Since frequency fluctuations are minimal over the duration of a single cycle, the fundamental component is calculated using a Single-Cycle Discrete Fourier Transform (SCDFT) [24]. Before applying the discrete transform, the continuous analog signal $i_A(t)$ is sampled by an Analog-to-Digital Converter (ADC). It is possible to assume that the system takes N samples per fundamental cycle T. The time t is replaced by discrete time steps $k\Delta t$, where $\Delta t = T/N$. The continuous signal $i_A(t)$ becomes a sequence of discrete samples as (1):

$$i_A[k] = i_A(k\Delta t) \text{ for } k = 0, 1, 2, \ldots, N-1. \quad (1)$$

The standard N-point Discrete Fourier Transform converts a time-domain sequence into frequency-domain components [25]. The formula for the n-th harmonic is determined by (2):

$$X[n] = \sum_{k=0}^{N-1} i_A[k] e^{-j\frac{2\pi}{N}nk}. \quad (2)$$

Since the hardware focuses exclusively on the fundamental frequency (50 Hz in proposed system), it is necessary only to determine the component where $n = 1$. The sum for the fundamental frequency becomes (3):

$$X[1] = \sum_{k=0}^{N-1} i_A[k] e^{-j\frac{2\pi}{N}k}. \quad (3)$$

Using Euler's formula ($e^{-j\theta} = \cos\theta - j\sin\theta$), this complex sum can be separated into its real and imaginary parts as (4), which correspond to orthogonal sine and cosine filters:

$$X[1] = \underbrace{\sum_{k=0}^{N-1} i_A[k] cos\left(\frac{2\pi}{N}k\right)}_{\text{Real Part}} \underbrace{- j\sum_{k=0}^{N-1} i_A[k] sin\left(\frac{2\pi}{N}k\right)}_{\text{Imaginary Part.}}. \quad (4)$$

The magnitude of the pure DFT sum, $X[1]$, is not equivalent to the RMS magnitude. Instead, it is a function of the sampling rate, equating to $\frac{N}{2}$ times the peak amplitude of the discrete sinusoid at the fundamental frequency [26,27]. To satisfy the requirements of the proposed mathematical model, this peak value must be translated into an RMS phasor ($I_{A,rms}$) by dividing by $\sqrt{2}$. This division stems directly from the Root Mean Square definition (5) for a continuous periodic function $f(t)$, where calculating the average of $sin^2\theta$ across a full period T mathematically yields $\frac{1}{2}$:

$$I_{rms} = \sqrt{\frac{1}{T}\int_0^T \left[I_{peak}^2 sin^2(\omega t)dt\right]} = \sqrt{I_{peak}^2 \frac{1}{2}} = \frac{I_{peak}}{\sqrt{2}}. \quad (5)$$

Combining (5), a scaling factor can be determined as (6):

$$\text{Scaling Factor } = \frac{2}{N} \cdot \frac{1}{\sqrt{2}} = \frac{\sqrt{2}}{N}. \tag{6}$$

By applying this scaling factor to the fundamental DFT sum, it is possible to arrive at the precise mathematical definition of the mapping $i_{\mathrm{A}}(t) \overset{\mathrm{SCDFT}}{\rightarrow} \mathbf{I}_{\mathrm{A}}$ as (7):

$$\mathbf{I}_A = \frac{\sqrt{2}}{N} \sum_{k=0}^{N-1} i_A(k\Delta t) e^{-j\frac{2\pi}{N}k}. \tag{7}$$

To make the math compatible with the complex exponential in the SCDFT, it is possible to rewrite a real cosine wave from (4) using Euler's identity $\cos(\theta) = \frac{e^{j\theta}+e^{-j\theta}}{2}$, as (8):

$$i_A(k\Delta t) = \frac{I_{peak}}{2}\left[e^{j(\frac{2\pi}{N}k+\phi_A)} + e^{-j(\frac{2\pi}{N}k+\phi_A)}\right]. \tag{8}$$

This shows that a real cosine wave is actually made of two complex vectors rotating in opposite directions: one at a positive frequency, and one at a negative frequency. After substitution of (8) into (7) the expanded description of the signal can be represented as (9):

$$\mathbf{I}_A = \frac{\sqrt{2}}{N}\frac{I_{peak}}{2} \sum_{k=0}^{N-1} \left[e^{j(\frac{2\pi}{N}k+\phi_A)} \cdot e^{-j\frac{2\pi}{N}k} + e^{-j(\frac{2\pi}{N}k+\phi_A)} \cdot e^{-j\frac{2\pi}{N}k}\right]. \tag{9}$$

After simplification in terms of positive $j\left(\frac{2\pi}{N}k+\phi_A\right) - j\frac{2\pi}{N}k = j\phi_A$ and negative $-j\left(\frac{2\pi}{N}k+\phi_A\right) - j\frac{2\pi}{N}k = -j\left(\frac{4\pi}{N}k+\phi_A\right)$ frequency, compound the (9) can be represented as (10):

$$\mathbf{I}_A = \frac{I_{peak}\sqrt{2}}{2N} \sum_{k=0}^{N-1} \left[e^{j\phi_A} + e^{-j(\frac{4\pi}{N}k+\phi_A)}\right]. \tag{10}$$

When evaluating the summation, the first term $e^{j\phi_A}$ of (10) acts as a constant independent of the index k, meaning that accumulating it over N samples simply scales it by N to yield $\sum_{k=0}^{N-1} e^{j\phi_A} = Ne^{j\phi_A}$. Conversely, the second term represents a complex sinusoid oscillating at exactly twice the fundamental frequency, as indicated by the $4\pi/N$ component in its exponent. Because this constitutes a perfectly balanced integer harmonic, summing it across exactly one full period N guarantees that the rotating vector cancels itself out entirely, resulting in $\sum_{k=0}^{N-1} e^{-j(\frac{4\pi}{N}k+\phi_A)} = 0$. As a result, it is possible to simplify the equation as (11):

$$\mathbf{I}_A = \frac{I_{peak}\sqrt{2}}{2N}\left[Ne^{j\phi_A} + 0\right] = \frac{I_{peak}}{\sqrt{2}}e^{j\phi_A} = I_{A,rms}e^{j\phi_A}. \tag{11}$$

Further mapping from instantaneous sampled values to fundamental harmonic phasors is defined as (12):

$$i_A(t) \overset{\mathrm{SCDFT}}{\rightarrow} \mathbf{I}_A,\ i_B(t) \overset{\mathrm{SCDFT}}{\rightarrow} \mathbf{I}_B,\ i_C(t) \overset{\mathrm{SCDFT}}{\rightarrow} \mathbf{I}_C. \tag{12}$$

The logic implemented by RPA terminal is exclusive to the fundamental harmonic and ensures that high-frequency transients and DC offsets are effectively suppressed. This selective filtering provides a stable and robust steady-state representation of the grid's operating conditions, isolating the primary power frequency from unwanted distortions.

2.3. Vector Analysis in Balanced and in SPGF Modes

In a balanced steady-state operating mode, the three-phase currents are characterized by symmetrical magnitudes and uniform angular separation. This relationship is defined by (13):

$$|\mathbf{I}_A| = |\mathbf{I}_B| = |\mathbf{I}_C| = I_{rms} \tag{13}$$

In this case, the angular displacement between the phases is strictly 120° or equals $\frac{2\pi}{3}$ radians. To quantify the geometric interaction and phase shift between any two phases i and j, it is necessary to define the reactive cross-product R_{ij}. Mathematically, this is the imaginary component of the complex product between one phasor and the complex conjugate of another (14):

$$R_{ij}^{raw} = \mathrm{Im}\left(\mathbf{I}_i \mathbf{I}_j^*\right), i, j = \{A, B, C\}, i \neq j. \tag{14}$$

By substituting the polar forms $\mathbf{I}_i = I_i e^{j\phi_i}$ and $\mathbf{I}_j^* = I_j e^{-j\phi_j}$, the expression expands to (15):

$$R_{ij} = \mathrm{Im}\left\{ I_i I_j e^{j(\phi_i \ \phi_j)} \right\} = I_i I_j \sin(\phi_i - \phi_j). \tag{15}$$

Here I_i, I_j are the RMS magnitudes of the respective phases and $\phi_i - \phi_j$ is the angular difference between them. In a perfectly balanced system, the cross-product between adjacent phases simplifies to a constant proportional to the square of the RMS current as (16):

$$R_{AB} = I_{rms}^2 \sin\left(120^\circ\right) = I_{rms}^2 \frac{\sqrt{3}}{2}. \tag{16}$$

To isolate asymmetry induced by a fault, the reactive asymmetry matrix $\boldsymbol{R}$ is constructed to quantify the deviation of phase cross-products from their nominal symmetrical values. An SPGF creates a geometric distortion—a skewed phasor triangle—where the phase angles and magnitudes no longer adhere to the 120° balance. This physical shift causes the reactive cross-products to diverge from the ideal baseline of $\frac{\sqrt{3}}{2} I^2$.

To extract stable diagnostic features without numerical complexity, the matrix $\boldsymbol{R}$ is constructed using a symmetrised mapping architecture ($R_{ji} = R_{ij}$) derived from the magnitude of these interphase cross-product changes [28]. This formats the system-wide skew into a structured arrangement for fault analysis as (17):

$$\mathbf{R} = \begin{bmatrix} 0 & R_{AB} & R_{AC} \\ R_{BA} & 0 & R_{BC} \\ R_{CA} & R_{CB} & 0 \end{bmatrix}. \tag{17}$$

Because the diagonal entries of $\boldsymbol{R}$ are strictly zero, the trace of the matrix is zero ($\mathrm{Tr}(\boldsymbol{R}) = 0$). Symmetrization guarantees that the resulting spectral decomposition yields entirely real eigenvalues, while the zero-trace property ensures that the eigenvalues sum to zero ($\lambda_1 + \lambda_2 + \lambda_3 = 0$). Consequently, the matrix contains both positive and negative real roots, allowing directional properties to be preserved. Calculating deviations from the ideal baseline can be represented by (18):

$$\Delta R_{ij} = R_{ij,measured} - R_{ij,ideal}. \tag{18}$$

To transform this system into a high-level diagnostic tool capable of identifying the warped phasor triangle, the characteristic eigenvalue problem is applied (19):

$$\mathbf{R}\mathbf{v}_k = \lambda_k \mathbf{v}_k, \quad |\lambda_{\mathrm{dom}}| = max(|\lambda_1|, |\lambda_2|, |\lambda_3|). \tag{19}$$

Physically, the three-phase current network can be envisioned as a geometric space where balanced load conditions maintain a symmetrical equilateral phasor structure. An SPGF acts as an asymmetric vector pull that warps this profile. The dominant eigenvalue λ_{dom} represents the mathematical "stretching" or absolute magnitude of this structural collapse, which functions essentially as a "Richter scale" for grid asymmetry.

To define a normalized metric for unidirectional geometric distortion, the VARAC index uses the Skewness Ratio (K_{VARAC}). Defined in (20), it expresses the relationship between the magnitude of the dominant eigenvalue and the total asymmetry of the system. To quantify the physical severity of the disturbance, the framework employs a Fault Intensity Indicator (Λ_{VARAC}), scaled to units of Amperes [A].

$$\Lambda_{VARAC} = \sqrt{|\lambda_{\text{dom}}|}\ , \quad [pu]K_{VARAC} = \frac{|\lambda_{\text{dom}}|}{\sum_{\mathbf{k=1}}^{\mathbf{3}}|\lambda_k|}, [A]. \tag{20}$$

Under balanced operating conditions, the eigenvalues of the reactive asymmetry matrix remain relatively uniform, causing the Skewness Ratio (K_{VARAC}) to maintain a low baseline (typically ≈ 0.5 due to the structural symmetry constraints of the matrix) subject only to stochastic load noise. Upon the occurrence of a fault, K_{VARAC} converges toward 1.0, signalling that the geometric distortion of the system is dominated by a single principal axis. The metrics Λ_{VARAC} and K_{VARAC} bridge the gap between mathematical abstraction and physical reality by mapping the spectral results back to an intuitive current value. By ensuring the fault magnitude exceeds a predefined operational noise floor, Λ_{VARAC} serves as a critical gatekeeper that prevents the system from triggering on minor, non-risky grid fluctuations. Synthesizing the previous derivations, the final decision logic for identifying a SPGF and determining its directional orientation is formalized in (21):

$$\begin{cases} \Lambda_{VARAC} > \Lambda_{Lim} \Longrightarrow \text{SPGF Detected} \\ sign(\lambda_{\text{dom}}) \Longrightarrow \text{Fault Direction} \end{cases}. \tag{21}$$

To guarantee the operational reliability of the proposed protection scheme, the decision threshold Λ_{Lim} serves as a robust mathematical boundary designed to filter out transient measurement errors and stochastic noise, ensuring that the relay protection and automation (RPA) terminal responds exclusively to authentic grid instabilities. Rather than being arbitrarily chosen, the specific operational parameters ($\Lambda_{\text{NO_FAULT}} = 5$ A and $\Lambda_{\text{FAULT}} = 20$ A) were rigorously validated by offline sensitivity analysis using a data set of 1000 Monte Carlo simulation runs under varying network configurations, severe load imbalances, and high noise levels [29]. This analysis demonstrated that under unfaulted operating conditions, the baseline current asymmetry floor behaves according to a Gaussian distribution with mean μ and standard deviation σ, allowing the lower threshold ($\Lambda_{\text{NO_FAULT}} = 5$ A) to be assigned to the $\mu + 3\sigma$ upper limit, which mathematically ensures that 99.73% of all extreme load unbalances and measurement noise are safely ignored [30]. In contrast, the upper threshold ($\Lambda_{\text{FAULT}} = 20$ A) defines the conservative lower bound of structural asymmetry typically observed during high-impedance faults, thereby establishing an explicit mathematically sound deadband between 5 A and 20 A that completely eliminates nuisance tripping while preserving high sensitivity to weak fault currents. Compounding this security, real-time monitoring of the rate of change in the Skewness Ratio K_{VARAC} along with the corresponding eigenvector weights provides a deep diagnostic track of the disturbance; if K_{VARAC} initiates near unity (1.0) and subsequently decays toward its baseline within a few fundamental cycles, the protective logic can actively differentiate between transient anomalies and permanent faults, thereby supporting adaptive, automated clearing and restoration functions.

3. Results

3.1. Realisation of the VARAC Algorithm

The effectiveness of the VARAC methodology was validated through extensive MATLAB R2016a simulations and implementation by SIEMENS TIA-Portal, utilizing a radial feeder topology integrated into a local DNU. The study specifically examined the algorithm's performance across various grounding configurations, including isolated, resistively grounded, and solidly grounded neutrals. Particular emphasis was placed on compensated networks (arc-suppression coils), where overcompensation traditionally hinders the sensitivity of conventional protection schemes.

Based on the mathematical model detailed in Section 2, the structural flow illustrated in Figure 5 defines the operational sequence of the VARAC methodology. The realization is divided into four primary functional stages: signal acquisition, geometric transformation, spectral feature extraction, and adaptive decision logic.

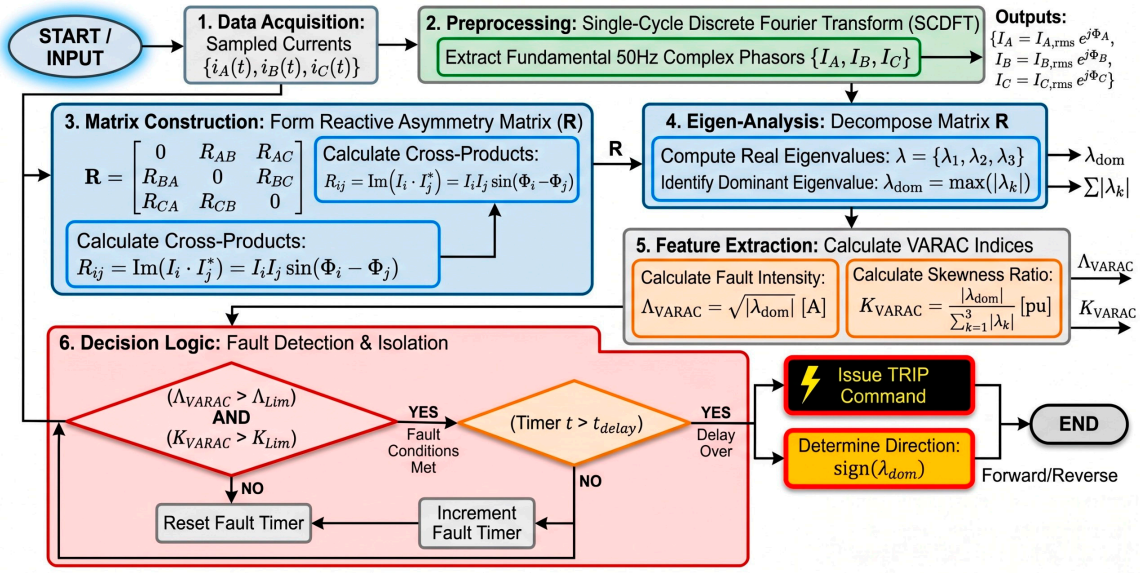


Figure 5. Representation of Structural Flow of the VARAC Methodology.

Initially, the algorithm performs high-speed data acquisition of the instantaneous phase currents $\{i_A, i_B, i_C\}$. To eliminate high-frequency noise and decaying DC components that typically plague traditional overcurrent relays during the first cycles of a fault, a Single Cycle Discrete Fourier Transform (SCDFT) is applied. This preprocessing step extracts the fundamental 50 Hz complex phasors, providing a clean steady-state representation of the grid's operating mode. The core of the VARAC mechanism lies in the Matrix Construction and Eigen-Analysis stages.

By processing the fundamental current phasors, the system computes the deviations of the reactive cross-products of the interphase to construct the symmetrised reactive asymmetry matrix $\boldsymbol{R}$. Unlike standard magnitude-based overcurrent detection, this matrix structure inherently captures the three-phase geometric vector relationships. The subsequent spectral decomposition yields three real eigenvalues due to the symmetric zero-trace matrix architecture. The dominant eigenvalue, λ_{dom}, is isolated as the principal indicator of system-wide geometric skew, effectively serving as a unique mathematical "fingerprint" of the ground fault.

To ensure high diagnostic reliability and secure operation, the algorithm synthesises two distinct decision features: the physical Fault Intensity Indicator (Λ_{VARAC}) scaled in Amperes and the dimensionless Skewness Ratio (K_{VARAC}) in units per unit. A TRIP command is executed only if the intensity and skewness thresholds (Λ_{Lim} and K_{Lim}) are

simultaneously exceeded for a duration longer than the programmable confirmation delay t_{delay}. This temporal validation provides robust immunity against transient, sub-cycle grid disturbances. Gleichzeitig, the polar sign of the dominant eigenvalue ($\text{sign}(\lambda_{\text{dom}})$), produces autonomous directional isolation, allowing the protective terminal to easily distinguish between internal (forward) and external (reverse) network faults.

3.2. Organisation of Measurement Equipment by SIPROTEC TIA-Portal

The hardware-software ecosystem designed for the realization of the VARAC algorithm is segmented into four primary functional modules:

- PLC-VARAC (CPU 1515-2 PN): The central processing unit serving as the main execution engine. It is responsible for the real-time processing of protection logic and the complex reactive asymmetry calculations.
- PC-Station (WinCC RT Professional): The Supervisory Control and Data Acquisition (SCADA/HMI) layer. This station handles high-level visualization, data logging, and operator control interfaces.
- PLC-Simulation (CPU 1515-2 PN): A dedicated emulation environment that replicates the dynamics of the primary power network. It is utilized to generate controlled single-phase short circuits, providing a safe and repeatable testbed for algorithm validation.
- PN/IE_1: The communication backbone utilizing a unified Profinet/Industrial Ethernet environment. This network ensures deterministic data exchange and synchronicity across all system nodes of the hardware–software system into a unified data exchange environment.

The integrated industrial network configuration, as established within the Siemens TIA Portal environment, is illustrated in Figure 6.

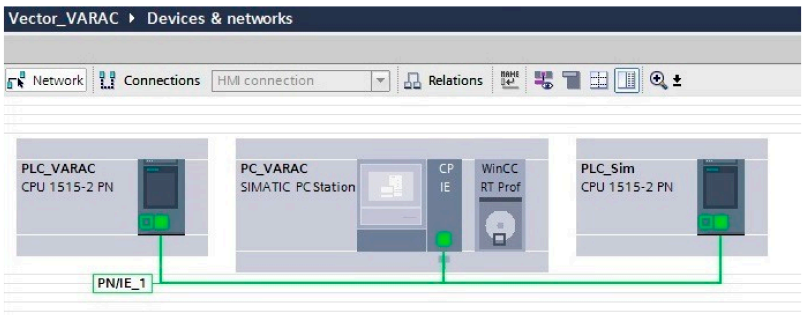
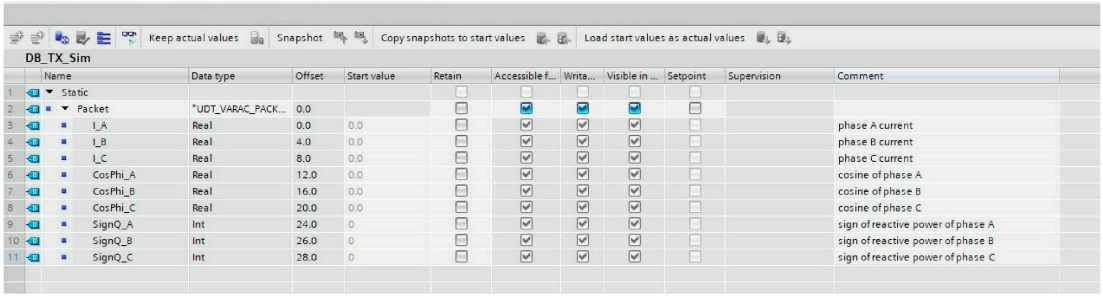


Figure 6. Structural Scheme of Hardware Components (PLC VARAC, PC Station and Simulation).

The structural integrity of the data transfer between the simulation environment and the protection controller is governed by the DB_TX_Sim data block, as shown in Figure 7.



	Name	Data type	Offset	Start value	Retain	Accessible f...	Write...	Visible in ...	Setpoint	Supervision	Comment
1	Static										
2	Packet	"UDT_VARAC_PACK...	0.0								
3	I_A	Real	0.0	0.0							phase A current
4	I_B	Real	4.0	0.0							phase B current
5	I_C	Real	8.0	0.0							phase C current
6	CosPhi_A	Real	12.0	0.0							cosine of phase A
7	CosPhi_B	Real	16.0	0.0							cosine of phase B
8	CosPhi_C	Real	20.0	0.0							cosine of phase C
9	SignQ_A	Int	24.0	0							sign of reactive power of phase A
10	SignQ_B	Int	26.0	0							sign of reactive power of phase B
11	SignQ_C	Int	28.0	0							sign of reactive power of phase C

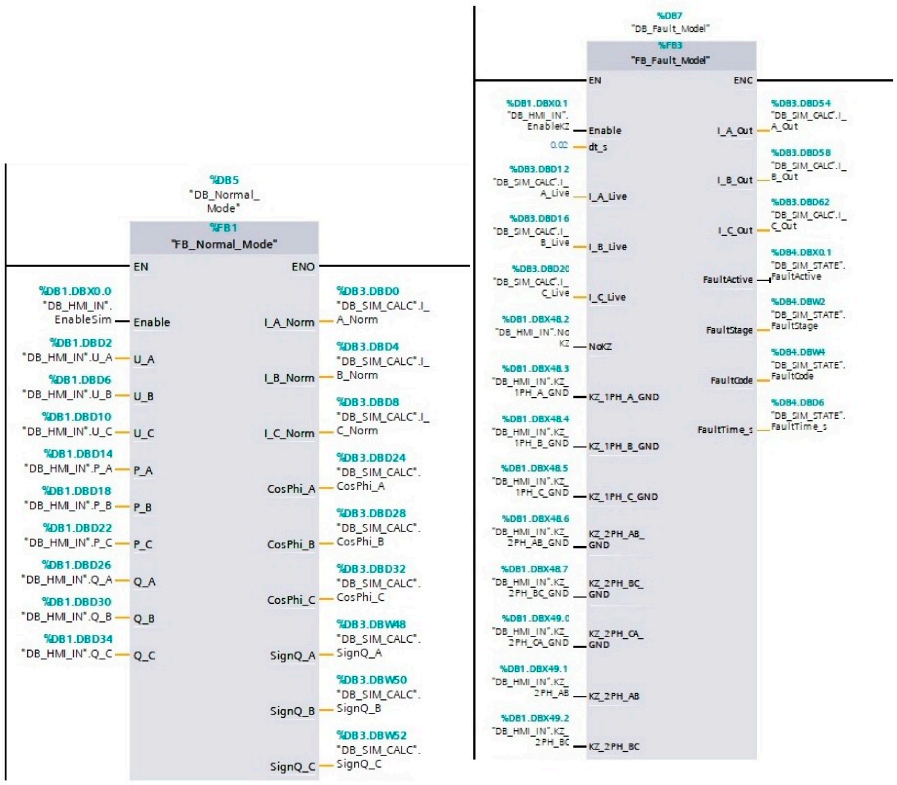
Figure 7. DB-Data Block PLC Sim: a PLC for signal generation that simulates input parameters in the substation switchgear.

This interface facilitates the transmission of a high-fidelity parameter packet essential for vector analysis, consisting of the following:

- Instantaneous phase currents: raw current magnitude data for phases A, B, and C.
- Phase Power Factors (cos ϕ): Measurements of individual power factors for each phase, allowing the algorithm to mathematically decompose the current into its active and reactive components.
- Reactive Power Signage (SignQ): Directional indicators for each phase that define the flow of reactive current, a critical variable for the directional isolation logic within the VARAC framework.

The software architecture, as illustrated in Figure 2, utilizes a Cyclic Interrupt Organization Block (OB) containing the Normal Mode Function Block (FB) as its core logical component [31].

This block processes primary input parameters—voltages (U_A, U_B, U_C), active powers (P_A, P_B, P_C), and reactive powers (Q_A, Q_B, Q_C)—streamed from the simulation environment. The output of FB consists of the calculated normalized currents (I_{norm}), the phase power factors (cos ϕ), and reactive power signs ($Sign$Q) for all three phases. These values serve as a high-fidelity steady-state baseline, enabling the VARAC algorithm to perform a comparative analysis in real time against instantaneous measurements to ensure a rapid and accurate detection of the onset of the fault. Figure 8b serves as the system's Fault Injection Engine, designed to simulate various grid disturbances—specifically SPGF within the TIA Portal environment. This block creates the "adversarial" conditions necessary to validate the K_{VARAC} skewness ratio and Λ_{VARAC} intensity thresholds. By triggering a specific fault via FB3, the system verifies that the main protection controller correctly identifies the fault type and respects the 100 ms trip delay.

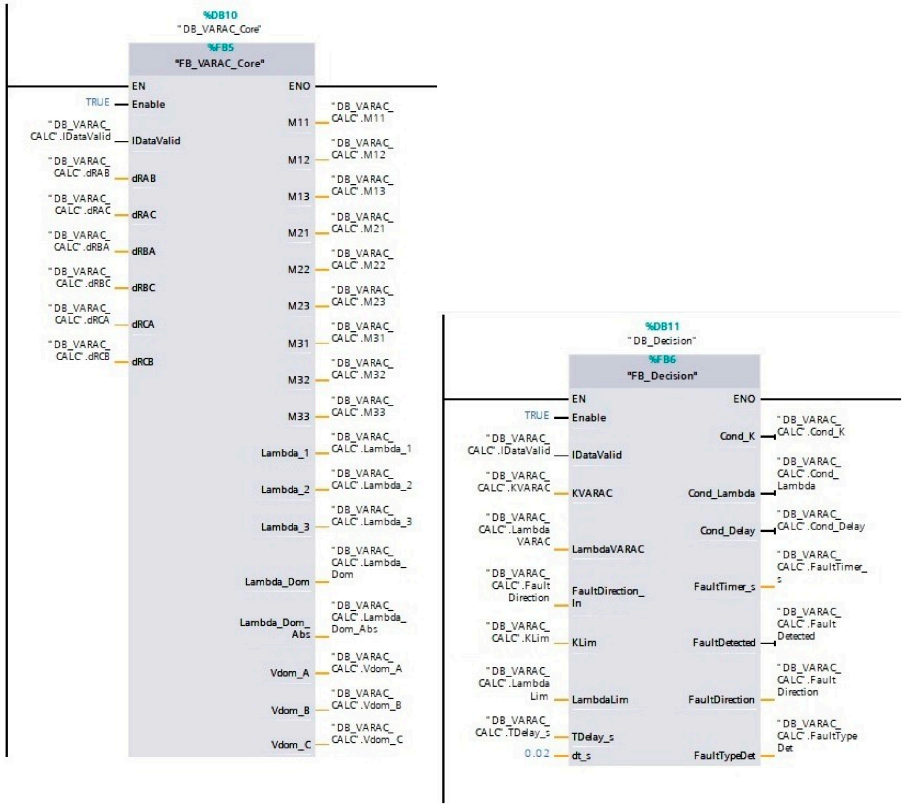


(**a**) (**b**)

Figure 8. Ladder Logic: Determination of power system parameters during normal and SPGF operating conditions. (**a**) FB: Normal Mode; (**b**) FB: SPGF Mode.

The implementation of the VARAC algorithm is partitioned into two primary functional modules within the TIA Portal environment: FB (VARAC_Core) and FB (Decision).

The VARAC Core Block executes the spectral decomposition of the reactive asymmetry matrix **R** (see Figure 9). It processes differential cross-products to compute the real eigenvalues of the system ($\lambda_1, \lambda_2, \lambda_3$) and the dominant eigenvector v_{dom}. This block isolates the dominant eigenvalue λ_{dom} to derive the intensity of the fault (Λ_{VARAC}) and identifies the specific fault phase by analysing the components of the normalised eigenvector. At the same time, the decision block serves as the logic arbiter, implementing the final decision gate. It assesses K_{VARAC} and Λ_{VARAC} against the predefined diagnostic thresholds K_{Lim} and Λ_{Lim}. To ensure immunity to transient disturbances, a confirmation timer (t_{delay}) must satisfy the temporal requirement before the FaultDetected flag is asserted. In addition, it uses the polarity of sign(λ_{dom}) to determine the directionality of the fault and provides fault-type classification for SCADA integration.



(**a**) (**b**)

Figure 9. Ladder Logic: Builds the VARAC working matrix, performs eigen-analysis, and computes λ, K_{VARAC}, Λ_{VARAC}, as well as the fault direction. (**a**) FB: VARAC Core. Analytical Processing and Feature Extraction (**b**) FB: Decision. Logic Arbitration and Fault Isolation.

3.3. Experimental Evaluation

The proposed VARAC protection framework was validated within a real-time RPA environment, utilizing a high-fidelity simulation engine to emulate various operational states. The transition from nominal steady-state operation to fault conditions demonstrates the algorithm's capability to detect structural asymmetries in the current-vector space.

Under nominal balanced conditions, the three-phase current phasors exhibit a high degree of geometric symmetry, as shown in the phasor diagram of Figure 10. The results indicate that the Fault Intensity Indicator remains at a negligible baseline (Λ_{VARAC} = 2.30 A), significantly below the established protection threshold (Λ_{Lim} = 60.00 A). The reactive asymmetry vector, I_{VARAC}, remains centered at the origin, confirming that the reactive

asymmetry matrix **R** generates eigenvalues of near-zero magnitude. This result validates the algorithm's robustness against stochastic load noise and its ability to maintain a stable pre-fault reference.

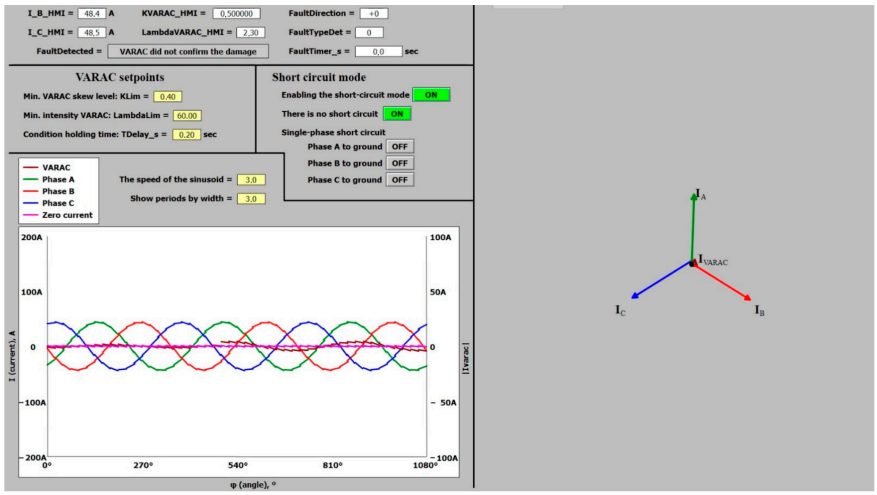


Figure 10. Vector Visualisation in TIA-portal. Normal Mode.

The inception of a SPGF introduces a severe geometric skew into the current–vector space. The VARAC algorithm successfully identifies the fault by monitoring the growth of the dominant eigenvalue magnitude and the alignment of the resulting asymmetry vector. Upon the activation of an SPGF on Phase A, the magnitude of the Phase A current increases, causing a directional shift in the phasor triangle. As evidenced in Figure 11, the fault intensity (Λ_{VARAC}) increases to 70.15 A, exceeding the trip threshold. The asymmetry vector I_{VARAC} aligns precisely with the Phase A axis, facilitating correct phase selection.

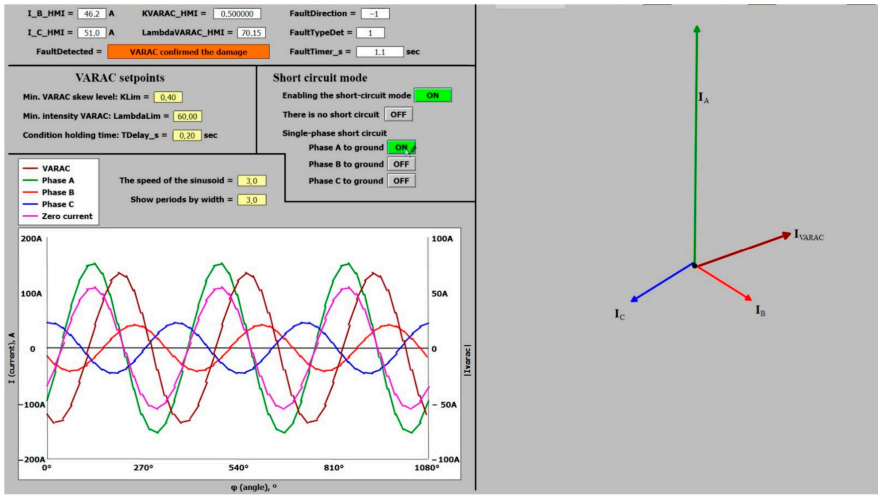


Figure 11. Vector Visualisation in TIA-portal. SPGF: Phase A.

The terminal asserted the FaultDetected status after the expiration of the confirmation timer (t_{delay} = 0.20 s).

The inception of an SPGF introduces a severe geometric skew into the current-vector space, warping the equilateral shape of the three-phase phasor triangle. The VARAC algorithm successfully identifies this disturbance by monitoring the growth of the absolute dominant eigenvalue $|\lambda_{\mathrm{dom}}|$ and tracking the spatial alignment of the resulting asymmetry vector. Upon the initiation of an SPGF in Phase A, this structural imbalance causes a sharp directional shift in the current-vector space (Table 1). As evidenced in Figure 11, the

calculated Fault Intensity Indicator (Λ_{VARAC}) rapidly increases to 70.15 A, safely exceeding the configured protection threshold Λ_{Lim} (60.00 A). Similarly, the asymmetry vector $\boldsymbol{I}_{\mathrm{VARAC}}$ aligns precisely along the Phase A axis, facilitating the correct and direct phase selection. The terminal asserted the FaultDetected status after the expiration of the programmable confirmation delay timer ($t_{\mathrm{delay}} = 0.20$ s), confirming secure, transient-free protection coordination.

Table 1. Performance Summary of VARAC Algorithm Across Simulated Grid States.

Operating Mode	Λ_{VARAC} [A]	K_{VARAC} [pu]	T_{trip} [s]	Decision Status
Normal (Balanced)	2.30	0.50	-	Standby
SPGF (Phase A)	70.15	1.0	0.2	TRIP (Confirmed)
SPGF (Phase B)	69.62	1.0	0.2	TRIP (Confirmed)
SPGF (Phase C)	69.15	1.0	0.2	TRIP (Confirmed)

3.4. Comparative Advantages of the VARAC Methodology

To establish the technical superiority, novelty, and practical viability of the proposed Vector Analysis of Reactive Asymmetry Current (VARAC) method, its performance is benchmarked at two distinct levels: first, against standard industrial relay protection and automation (RPA) schemes widely deployed in distribution networks, and second, against contemporary state-of-the-art (SOTA) research frameworks published in the recent literature.

Traditional single-phase-to-ground fault (SPGF) protection schemes often struggle to maintain selectivity and sensitivity simultaneously, particularly in networks with resonant grounding via Arc-Suppression Reactors (ASRs). Table 2 highlights the performance envelope of the proposed VARAC method compared to classic industrial schemes, including Zero-Sequence overload ($3I_0$), Directional Wattmetric/Varmetric, admissibility-based protection (Y_0), and standard transient/wavelet-based protection.

Table 2. Comparative evaluation of VARAC against standard industrial SPGF protection schemes.

Methodology	Sensitivity to R_f	ASR Tuning Dependence	Transient Influence	Implementation Cost
Zero-Sequence Overcurrent (3I0) [32]	Very Low (<100 Ω)	High (Fails when compensated)	Highly susceptible	Low
Directional Wattmetric/Varmetric [33]	Low (<500 Ω)	Moderate	High transient errors	Moderate
Admittance-based (Y_0) [34]	Moderate (<1000 Ω)	Low	Susceptible to noise	Moderate
Transient/Wavelet-based [35,36]	High (>2000 Ω)	Independent	Requires high sampling rate	Very High
Proposed VARAC	Very High (>5000 Ω)	Low (Self-compensating)	Filtered by SCDFT	Low (Runs on standard PLCs)

As demonstrated in Table 2, while traditional zero-sequence overcurrent and directional power methods suffer from low sensitivity and high dependence on ASR tuning parameters, transient/wavelet-based schemes offer high sensitivity. However, these transient schemes require high-frequency sampling analogue-to-digital converters (ADCs) and dedicated digital signal processors (DSPs), making them economically unfeasible for widespread, cost-sensitive distribution network units (DNUs).

The proposed VARAC method successfully bridges this gap. Using standard Single-Cycle Discrete Fourier Transform (SCDFT) algorithms running inside cyclic interrupts (e.g., OB30 on standard PLCs), it filters high-frequency transient noise and operates at a low hardware implementation cost while still achieving exceptional sensitivity to high-impedance faults (HRFs) up to 5000 Ω.

In addition to outperforming standard industrial protections, VARAC introduces a fundamental divergence in detection principles compared to state-of-the-art methods in the recent literature. While contemporary authors rely heavily on transient energy or multi-point power flow analysis, VARAC exploits the geometric asymmetry of the reactive current vectors.

Table 3 provides a technical benchmark that compares VARAC directly with the transient-based method of Wei et al. (2022) [4,14] and the negative-sequence power directional method of Özveren & Usta (2023) [17].

Table 3. Technical Comparison: VARAC vs. SOTA Research Schemes.

Methodology	Core Principle	Key Advantages	Limitations
Proposed VARAC	Eigen-analysis of reactive asymmetry matrix ($\boldsymbol{R}$)	Very high sensitivity (up to 5000 Ω); highly robust in compensated networks; localized processing	Thresholds benefit from adaptive tuning under severe topology changes
Wei et al. (2022) [4]	Transient energy & cosine similarity metrics	Clear quantitative fault probability; highly effective for radial feeders; IEEE 34-bus validated	Performance significantly degrades with high grounding resistance ($R_f > 1000$ Ω)
Özveren & Usta (2023) [17]	Negative sequence reactive power direction	Fast tripping in active networks; unit-based selective isolation	Requires bi-directional sensors and synchronized measurements at multiple grid nodes

Note: VARAC prioritizes geometric current field distortion over absolute magnitude or high-frequency transient energy spectral density.

The primary advantage of the VARAC framework over the schemes in the contemporary literature lies in its physical robustness under adverse network conditions. For instance, the transient energy approach proposed by Wei et al. [4] is highly sensitive in low-impedance scenarios, but its performance rapidly degrades under high-impedance faults (above 1000 Ω) due to the severe damping of transient signals of high frequency. In contrast, VARAC maintains a selectivity accuracy of more than 98% even at 5000 Ω by focusing on reactive asymmetry of the fundamental frequency of the steadyy state. Furthermore, in resonant-grounded networks, the reliance of VARAC on geometric skewness (K_{VARAC}) guarantees reliable fault feeder identification even when zero-sequence capacitive currents are largely neutralised by ASRs.

Architecturally, the VARAC method offers superior operational autonomy. Unlike power-based schemes (e.g., Özveren & Usta [17]) that mandate a complex, communication-heavy network of bi-directional sensors across multiple feeder terminals, VARAC is fully optimised for localised deployment on standard industrial controllers. This enables utilities to achieve high-fidelity diagnostic performance on existing hardware assets without

requiring expensive fibre-optic synchronisation infrastructure, effectively bridging the gap between advanced theoretical diagnostics and practical field application.

4. Practical Implementation Challenges and Solutions

Deploying the VARAC framework in an active automated process control system (APCS) environment presents several engineering challenges that must be addressed to preserve its mathematical sensitivity:

1. Current Transformer (CT) Angle Errors at Low Currents: Under high-resistance faults, zero-sequence currents can drop below 1 A. At these low magnitudes, conventional core-balance CTs suffer from significant phase-angle errors (up to 5°–10°), which can compromise vector calculation. To mitigate this, a software-based phase-compensation table is integrated directly into the PLC Functional Block (FB). This FB dynamically adjusts the calculated angle of the vector based on the measured current magnitude using pre-calibrated CT excitation curves.
2. PLC Computational Limits and Sampling Synchronization: Running a continuous SCDFT inside a fast Cyclic Interrupt Organisation Block (e.g., OB30 with a cycle time of 1 ms) can strain standard PLC CPUs. To optimise execution, the SCDFT is calculated using a sliding-window array of 20 samples per cycle (at a sampling rate 1 kHz. Real-world tests on an industrial S7-1500 controller showed that this execution consumes less than 8% of the cyclic processing capacity, leaving ample margins for auxiliary SCADA communications.
3. Communication Latency in Hierarchical RPA Environments: Because the preselective stage operates hierarchically (transmitting metadata from local feeder terminals to a central gateway), network latency could delay fault localisation. This is resolved by keeping the initial detection localised at the feeder terminal Unit (DNU) level, which instantly triggers an event flag. The higher-level central SCADA system then asynchronously queries the vector profiles for diagnostic logging and post-fault topology optimisation, ensuring that detection latency is decoupled from network communication delays.

5. Conclusions

This research presents the Vector Analysis of Reactive Asymmetry (VARAC) method, a novel single-phase-to-ground fault (SPGF) detection and directional isolation framework designed for medium-voltage (6–35 kV) distribution networks. Moving away from conventional error-prone zero-sequence amplitude monitoring, the proposed methodology employs the spectral decomposition of a symmetrised reactive asymmetry matrix R to isolate geometric distortions in the three-phase current field. This mathematical shift successfully eliminates any reliance on highly unstable zero-sequence currents. Rigorous sensitivity analysis confirmed that the decision threshold (Λ_{Lim}) remains mathematically robust in diverse operating environments, preserving a reliable selectivity margin even under conditions of severe feeder phase unbalance or a $\pm$10% detuning of Arc-Suppression Reactors (ASRs). Although the exclusive focus on SPGFs is physically and economically warranted—given that standard phase overcurrent relays easily clear multi-phase short circuits whereas low-current SPGFs represent 70–80% of all distribution grid anomalies—the algebraic core of VARAC remains highly extensible. The reactive asymmetry matrix structure can be readily adapted to identify and classify other multi-phase asymmetrical faults by analysing negative- and zero-sequence reactive current trajectories. Measurement inaccuracies under low-current regimes are dynamically compensated via a software-based lookup table integrated directly inside the Programmable Logic Controller (PLC) Function Block, preserving high directional sensitivity. The algorithms are computationally optimised to

run within a standard Cyclic Interrupt Organisation Block (OB30) on a Siemens S7-1500 controller, consuming less than 8% of CPU processing capacity. Communication bottlenecks are mitigated through a hierarchical architecture where time-critical tripping and localised detection reside at the Distribution Network Unit (DNU) level, while non-urgent diagnostic data are asynchronously uploaded to the supervisory SCADA system.

Future research will focus on the deployment of adaptive, self-tuning threshold algorithms that dynamically adjust to active grid topology reconfigurations (such as automatic loop closures) and conducting extensive physical validations using hardware-in-the-loop (HIL) real-time digital simulators (RTDS).

Author Contributions: Conceptualization, B.O., V.R. and D.K.; methodology, B.O., V.R. and D.K.; software, Z.I. and B.I.; validation, Z.I. and D.B.; formal analysis, B.I. and O.T.; investigation, Z.I. and B.I.; resources, O.T. and D.B.; data curation, Z.I., B.I. and O.T.; writing—original draft preparation, B.O., D.B., V.R. and D.K.; writing—review and editing, B.O., V.R. and D.K.; visualization, Z.I., B.I. and D.B.; supervision, B.O., V.R. and D.K.; project administration, B.O., V.R. and D.K.; funding acquisition, Z.I. All authors have read and agreed to the published version of the manuscript.

Funding: The paper was prepared with the support of the Ministry of Education and Science of the Republic of Kazakhstan (grant No. AP23486411).

Institutional Review Board Statement: Not applicable.

Informed Consent Statement: Not applicable.

Data Availability Statement: The research data is presented in the article.

Acknowledgments: The authors have reviewed and edited the output and take full responsibility for the content of this publication.

Conflicts of Interest: The authors declare no conflicts of interest.

Abbreviations

The following abbreviations are used in this manuscript:

SPGF	Single-phase-to-ground faults
VARAC	Vector Analysis of Reactive Asymmetry Current
RPA	Relay Protection and Automation
APCS	Automated Process Control System
ASR	Arc-suppression Reactor
DNU	Distribution Network Unit
PLC	Programmable Logic Controller
ADC	Analog-to-Digital Converter
SCDFT	Single-Cycle Discrete Fourier Transform
RMS	Root Mean Square
DC	Direct Current
OB	Cyclic Interrupt Organization Block
FB	Functional Block
SCADA	Supervisory Control and Data Acquisition

References

1. Zaporozhets, A.; Babak, V.; Kostenko, G.; Zgurovets, O.; Denisov, V.; Nechaieva, T. Power system resilience: An overview of current metrics and assessment criteria. In *Systems, Decision and Control in Energy VI: Volume I: Energy Informatics and Transport*; Springer: Berlin/Heidelberg, Germany, 2024; pp. 35–58.
2. Horowitz, S.H.; Phadke, A.G.; Henville, C.F. *Power System Relaying*, 5th ed.; John Wiley & Sons: Hoboken, NJ, USA, 2022; 528p, ISBN 978-1-119-83843-2.

3. Knapp, E.D. *Industrial Network Security: Securing Critical Infrastructure Networks for Smart Grid, SCADA, and Other Industrial Control Systems*; Elsevier: Amsterdam, The Netherlands, 2024.
4. Wei, X.; Wang, X.; Gao, J.; Yang, D.; Wei, K.; Guo, L. Faulty Feeder Detection for Single-Phase-to-Ground Fault in Distribution Networks Based on Transient Energy and Cosine Similarity. *IEEE Trans. Power Deliv.* **2022**, *37*, 3968–3979. [CrossRef]
5. Zhantlessova, A.; Issabekova, B.; Issabekov, Z. Determination of Earth Faults in Cable Lines with Insulated Neutrals. In Proceedings of the 2025 International Ural Conference on Electrical Power Engineering (UralCon), Magnitogorsk, Russia, 25–28 September 2025; pp. 346–351. [CrossRef]
6. Issabekov, Z.; Novozhilov, A.N.; Novozhilov, T.A.; Issabekova, B.B. Protection of two-cable line from single phase-to-earth fault with absolute selectivity. *News Natl. Acad. Sci. Repub. Kazakhstan* **2018**, *431*, 128–132. [CrossRef]
7. Issabekov, Z.B.; Novozhilov, A.N.; Issabekova, B.B.; Anarbayev, A.Y. Configurations of 6-10 kV cable lines and types of cable damages. *Thermophys. Basis Energy Technol. (TBET 2020)* **2021**, *2337*, 030002. [CrossRef]
8. Novozhilov, A.; Issabekov, Z.; Novozhilov, T.; Issabekova, B.; Tyulyugenova, L. Absolutely Selective Single-Phase Ground-Fault Protection Systems for Bunched Cable Lines. *Electricity* **2026**, *7*, 2. [CrossRef]
9. Novozhilov, A.; Issabekov, Z.; Novozhilov, T.; Issabekova, B.; Tyulyugenova, L. Single-Phase Earth-Fault Protection of Power Cable of a Salt-Producing Floating Platform. *Energies* **2025**, *18*, 5234. [CrossRef]
10. Yesmakhanova, L.; Issabekov, Z.; Issabekova, B.; Ordabayev, B.; Zhantlessova, A.; Kudabaev, D.; Talipov, O. An IoT-Based Technique for Detecting Single-Phase Earth Faults in 6–35 kV Cable Lines Using Current Sensors. *Eng* **2026**, *7*, 256. [CrossRef]
11. Chaban, A.; Lis, M.; Szafraniec, A.; Levoniuk, V. Mathematical Modelling of Transient Processes in a Three Phase Electric Power System for a Single Phase Short-Circuit. *Energies* **2022**, *15*, 1126. [CrossRef]
12. Jetpissov, M.; Tergemes, K.; Sheryazov, S.; Berdibekov, A.; Smailova, G.A. Selective method for identifying single-phase ground faults with transient resistance in isolated neutral medium-voltage networks. *Energies* **2025**, *18*, 5699. [CrossRef]
13. Ustinov, D.; Nazarychev, A.; Pelenev, D.; Babyr, K.; Pugachev, A. Investigation of the effect of current protections in conditions of single-phase ground fault through transient resistance in the electrical networks of mining enterprises. *Energies* **2023**, *16*, 3690. [CrossRef]
14. Zhang, S.; Cai, Y.; Li, Y.; Wu, H.; Li, Z.; Li, Z. Protection Scheme for Distribution Network Ground Fault Based on Comparison of Zero Sequence Magnitude. *Res. Sq.* **2025**. [CrossRef] [PubMed]
15. Ren, J.; Zhang, Z.; Jing, S.; Lee, W.J. Zero-Sequence Current Retrieval based Robust High-Impedance Fault Location in Resonant Grounding System. *IEEE Trans. Instrum. Meas.* **2025**, *74*, 3555413. [CrossRef]
16. Pujari, R.; Alam, M.N. Review on distance relaying for the protection of modern power system networks. *IEEE Access* **2025**, *13*, 28861–28893. [CrossRef]
17. Özveren, F.; Usta, Ö. A power based integrated protection scheme for active distribution networks against asymmetrical faults. *Electr. Power Syst. Res.* **2023**, *218*, 109223. [CrossRef]
18. Muñoz-Arango, G.; Mora-Flórez, J.; Pérez-Londoño, S. A power-based fault direction estimation method for active distribution networks. *Results Eng.* **2024**, *21*, 101754. [CrossRef]
19. Zhu, H.; Wang, X.; Fan, C.; Hu, Y.; Tai, N. Positive sequence reactive current differential protection of transmission lines connected to energy storage power station. *Front. Energy Res.* **2025**, *13*, 1666514. [CrossRef]
20. Phadke, A.G.; Thorp, J.S. *Computer Relaying for Power Systems*, 2nd ed.; John Wiley & Sons: Hoboken, NJ, USA, 2009; 344p, ISBN 978-0-470-74757-5.
21. Siemens. *SIPROTEC 5, Fault Recorder 7KE85*; Siemens: Munich, Germany, 2025.
22. Benedetto, J.J.; Ferreira, P.J. *Modern Sampling Theory: Mathematics and Applications*, 1st ed.; Springer Science & Business Media: Berlin, Germany, 2012.
23. Theraja, B.; Theraja, A. *ABC of Electrical Engineering: Cover Basic Electrical Engineering and Electrical Machines for Ist Year Students of BE (All Branches), B. Tech and AIME*; S. Chand Publishing: New Delhi, India, 2012; 456p.
24. Vercruysse, A.; Miller, M.W.; Brake, J.; Harris, D. A Tutorial-style Single-cycle Fast Fourier Transform Processor. In Proceedings of the Great Lakes Symposium on VLSI, Irvine, CA, USA, 6–8 June 2022; Volume 2022, pp. 525–530. [CrossRef]
25. Jena, S.K. *Fourier, Laplace, and the Tangled Love Affair with Transforms: The Art of Signal Synthesis and Analysis*; Springer Nature: Berlin/Heidelberg, Germany, 2025; p. 537. ISBN 978-3031801648.
26. Serbes, A. Fast and Efficient Sinusoidal Frequency Estimation by Using the DFT Coefficients. *IEEE Trans. Commun.* **2019**, *67*, 2333–2342. [CrossRef]
27. Mondal, D.; Chakrabarti, A.; Sengupta, A. *Power System Small Signal Stability Analysis and Control*; Academic Press: Cambridge, MA, USA, 2020.
28. Arias-Esquivel, Y.; Cárdenas-Dobson, R.; Uriarte, M.; Díaz, M.; Tarisciotti, L. An Advanced Zero-Error Continuous Control Set Model Predictive Controller for Low Voltage Ride Through of Grid-Connected Power Converters. *IEEE Trans. Ind. Electron.* **2026**, *73*, 682–693. [CrossRef]

29. Schneider, G. *Die Monte Carlo Simulation: Was ist Darunter zu Verstehen, Welche Instrumente für die Anwendung Werden Benötigt und der Stellenwert Verdeutlicht Anhand Eines Beispiels*; GRIN Verlag: Munich, Germany, 2011.
30. Rajan, D. Probability, Random Variables, and Stochastic Processes. In *Mathematical Foundations for Signal Processing, Communications, and Networking*; CRC Press: Boca Raton, FL, USA, 2017; pp. 205–244.
31. Siemens. *SIMATIC, Ladder Logic (LAD) for S7-300 and S7-400 Programming, 03.2025*; Siemens: Munich, Germany, 2006.
32. Mooney, J.; Peer, J. Application guidelines for ground fault protection. In Proceedings of the 24th Annual Western Protective Relay Conference, Spokane, WA, USA, 21–23 October 1997.
33. Roberts, J.; Hou, D.; Calero, F.; Altuve, H.J. *New Directional Ground-Fault Elements Improve Sensitivity in Ungrounded and Compensated Networks*; Technical Paper; Schweitzer Engineering Laboratories: Pullman, WA, USA, 2001; pp. 1–27.
34. Wahlroos, A.; Altonen, J. Compensated networks and admittance based earth-fault protection. In *Proceedings of the Seminar on Methods and Techniques for Earth Fault Detection, Indication and Location*; Kaunas University of Technology: Kaunas, Lithuania; Aalto University: Espoo, Finland, 2011.
35. Liu, D.; Dy'sko, A.; Hong, Q.; Tzelepis, D.; Booth, C.D. Transient wavelet energy-based protection scheme for inverter-dominated microgrid. *IEEE Trans. Smart Grid* **2022**, *13*, 2533–2546. [CrossRef]
36. Gong, J. Wavelet packet coefficient of transient first half wave line selection method for single-phase grounding fault. In *Proceedings of the IOP Conference Series: Earth and Environmental Science*; IOP Publishing: Bristol, UK, 2022; Volume 983, p. 012012.

Disclaimer/Publisher's Note: The statements, opinions and data contained in all publications are solely those of the individual author(s) and contributor(s) and not of MDPI and/or the editor(s). MDPI and/or the editor(s) disclaim responsibility for any injury to people or property resulting from any ideas, methods, instructions or products referred to in the content.